Evaluation of Cloud Type Occurrences and Radiative Forcings Simulated by a Cloud Resolving Model Using Observations from Satellite and Cloud Radar

Y. Luo and S. K. Krueger
University of Utah
Salt Lake City, Utah

Introduction

Because of both the various effects clouds exert on the earth-atmospheric system and the cloud feedback, correct representations of clouds in numerical models are critical for accurate climate modeling and weather forecast. Unfortunately, determination of clouds and their radiative feedback processes is still the weakest component of current general circulation models (e.g., Senior and Mitchell 1993, Cess et al. 1996).

Using radiative fluxes at the top of atmosphere (TOA) available from satellite observations made by the Earth Radiation Budget Experiment (ERBE; Barkstrom 1984), one could assess cloud radiative effects observed by the satellites (e.g., Harrison et al. 1990), and the ability of general circulation models to represent these effects could be assessed by comparing the simulated cloud radiative effects at the TOA, caused by all clouds as a whole, to that from satellite observations (e.g., Kiehl et al. 1994, Chen and Erich 1995). However, the agreement between model's simulation and satellite observations could be due to the presence of compensating errors associated with different cloud types.

Data products from the International Satellite Cloud Climatology Project (ISCCP; Rossow and Schiffer 1991, Rossow et al. 1996, Rossow and Schiffer 1999) provide retrievals of cloud amount, cloud optical depth, and cloud top pressure, i.e., information for defining various cloud types. These products have been used widely for evaluating the representation of clouds in large-scale numerical models and for better understanding effects of various cloud types, defined by cloud top pressure and optical depth, on the TOA radiation budget (e.g., Hartmann et al. 1992, Chen et al. 2000, Webb et al. 2001, Hartmann et al. 2001, Zhang et al. 2001).

Cloud-resolving models (CRMs) are increasingly being used for understanding cloud processes and for better representing these processes in large-scale models (e.g., Chaboureau and Bechtold 2002, Khairoutdinov and Randall 2001, Kohler 1999, Krueger et al. 1995). However, detailed evaluations of the ability of CRMs to represent the occurrence of various cloud types have not been made mainly due to lack of observations on comparable spatial and temporal resolution.

During the past decade, detailed observations of clouds and radiation have increased. The long-term high time-resolution cloud radar (and other) observations at the Atmospheric Radiation Measurement (ARM) Cloud and Radiation Testbed (CART) sites have provided information for cloud, atmosphere,

and radiative flux. Algorithms have been developed to retrieve macrophysical and microphysical properties of clouds from ground-based measurements (e.g., Dong and Mace 2003, Wang and Sassen 2002a, Mace et al. 2001). On the other hand, cloud properties for large spatial and temporal domains are now available from satellite observations with spacial resolution on the order of one to several kilometer(s) every half-hour using advanced retrieval methods (e.g., Platnick et al. 2001, Han et al. 1999, Minnis et al. 1998, Minnis et al. 1995a and 1995b). These datasets make it possible to determine and evaluate the occurrence frequencies and radiative forcings of various cloud types in a CRM (or single-column model [SCM]/general circulation model) simulation.

Observations

In this study, observations from the millimeter wave cloud radar (MMCR) located at the ARM Southern Great Plains (SGP) Central Facility (CF) and from the satellite retrievals over the SGP CART site provided by Patrick Minnis' group at National Aeronautics and Space Administration (NASA) Langley Research Center are used to evaluate the occurrences (and radiative forcings) of various cloud types simulated by a CRM. Short descriptions of both datasets follow.

Observations from the Millimeter Wave Cloud Radar

The MMCR is a vertically pointing, single-polarization radar that operates at a frequency of 35 GHz (λ = 8.7 mm). The radar possesses a Doppler capability that will allow the measurement of cloud constituent vertical velocities. To optimize the radar for sensitivity, spatial resolution, and a reduction of range side-lobe artifacts the MMCR uses four operational modes. The most sensitive modes can detect reflectivity values approaching -50 dBZ. The MMCR probes the extent and composition of clouds, and also measures radar reflectivity of the atmosphere up to 20 km. The time-resolution of MMCR is about 39 sec. for all four operating modes. Depending on the mode in use, the MMCR has a vertical range gate resolution of 45 m and 90 m and a range distance from 0.1 km to 15 km. By using a narrow beam width of 0.2° to 0.3°, the MMCR has a horizontal field of view of 35m to 50 m at a height of 10 km. Observations from the MMCR have been used to evaluate hydrometer prediction by a global model. Weaknesses present in the MMCR include its availability at a single point within the SGP site, i.e., SGP CF (latitude 36.61°N, longitude 97.49°W), that it can detect objects other than clouds such as insects, and that it is unable to detect the smallest cloud particles (approximately $r_e \leq 4.0$ μm) (Wang and Sassen 2002b). Since the un-detected smallest cloud particles are radiatively insignificant, the MMCR is useful for studying the microphysical properties of most cloud layers. A micropulse lidar (MPL) can distinguish clouds from insects so that it is used together with the MMCR merged moments to detect boundary layer clouds.

Combining the MMCR reflectivity with other information, Mace et al. (2001; MCA hereafter) retrieved microphysical properties including ice water path (IWP), layer mean effective radius (r_e), and number concentration of ice crystals, of single-layer thin cirrus clouds over the SGP site since November 1996. The high time resolution (3 min averages every 8 min) and long-term coverage make these retrievals useful for evaluating the representation of cirrus clouds in atmospheric numerical models (Luo et al. 2003). The weaknesses include its availability at a single point and for only one cloud type.

Satellite Observations

Satellite observations we used include both the radiative fluxes at the TOA from geostationary operational environmental satellite-8 (GOES-8) and cloud products generated by Patrick Minnis' group at NASA Langley Research Center. The broadband longwave (LW) flux was obtained by conversion from narrow band LW radiance. The monthly mean uncertainty (rms error) is within 10 W/m^2 over the SGP SCM analysis domain (Khaiyer et al. 2002). The pixel level OLR has good quality too, although satellite navigation errors result in pixel shifts of 4- to 8-km. The reflected shortwave (SW) flux is calculated from broadband albedo, whose monthly mean uncertainty (rms error) is within 0.02 over the SGP SCM analysis domain based on the results from Khaiyer et al. (2002). Geostationary satellite cloud products are useful because they include cloud information over a large spatial domain at 4-km space resolution and at half-hour time intervals for all cloud types, so that occurrences, properties, radiative effects, and spatial distributions of various cloud types can be analyzed. Their disadvantages include the varying reliability of the retrievals. One source of uncertainties in satellite retrievals is the assumptions made about the cloud, atmosphere, and surface characteristics. The most important assumptions include: (1) cloud optical properties are uniform over the image pixels; hence, cloud cover of pixel is either zero or one and (2) clouds are single layers.

Minnis' group used a pair of multi-spectral algorithms, the visible infrared solar-infrared split-window technique (VISST) for daytime and Solar Infrared Station (SIRS) method for nighttime, as described by Minnis et al. (1995a) using the models of Minnis et al. (1998), together with the technique of Minnis and Smith (1998) to analyze the half-hourly, 4-km GOES-8 imager data (0.65 µm, visible [VIS]; 3.9 µm, solar infrared [SIR]; 10.8 µm, infrared [IR]; and 12.0 µm, split-window [SWC]). The ISCCP retrieval used a VIS-IR bispectral method in daytime and an IR-only method in nighttime so that cloud optical properties could not be retrieved for nighttime. The multi-spectral algorithms use radiative radiances at two more channels: the SIR radiance to estimate cloud particle size and the SWC radiance to help determine cloud phase (Young et al. 1997).

Minnis uses the general approach for quantifying clouds, which consists of two stages: cloud identification and cloud properties retrieval. Cloud is identified by comparing an observed radiance or set of radiances at different wavelengths to the values expected from a clear (cloudless) scene (pixel). If the observed radiance is sufficiently different from the clear-sky value, the pixel is designated as cloudy. For each cloudy pixel, variables including cloud phase, cloud top temperature, cloud optical depth, effective droplet radius (r_e) or effective ice crystal diameter (D_e), and liquid water path (LWP) or ice water path (IWP) are determined iteratively by matching the observed radiances with results from radiative transfer models and cloud microphysical models for a wide range of particle sizes and cloud and clear-sky temperatures. Minnis uses the profiles of temperature and humidity from the Rapid Update Cycle (RUC) 3 hourly soundings. In this study we used the Minnis cloud products over the ARM SGP Cloud and Radiation Testbed (CART) site during the summer 1997 intensive observation period (IOP). There are about 7000 pixels every half hour within the SGP SCM analysis domain.

Occurrence Frequency of Various Cloud Types

The effects of clouds on the earth-atmosphere system's radiative budget (and hydrological cycle) are different for various cloud types. The net radiative effect of clouds depends on cloud type occurrence

frequencies. We used the Minnis satellite retrievals within the SGP SCM analysis domain, together with the MMCR observations at the SGP CF, to evaluate the cloud type occurrence frequencies in a simulation performed by the UCLA/CSU CRM using the ARM variational analyses.

Methods for Analyzing Cloud Occurrences

Based on the Minnis half-hourly pixel level cloud products including cloud phase, cloud-top pressure, and cloud visible optical depth, we calculated the occurrence frequencies of various cloud types, as defined by total cloud visible optical depth and cloud-top pressure of highest cloud layer, at nearly half-hour intervals. The occurrence frequency of a cloud type is the fraction of the total number of pixels occupied by the cloud type within the SGP SCM analysis domain.

The ISCCP simulator was developed by S. Klein (GFDL) and M. Webb (UKMO) as a connection between results from a general circulation model/SCM and observations from satellite and single-point ground-based instruments. The ISCCP simulator divides a general circulation model/SCM predicted grid-mean cloud water/ice content at each level into a number of sub-grid columns using the profile of model cloud fraction together with a cloud overlap assumption. Each sub-grid column is considered as either clear or containing a single cloud layer, similar to a satellite pixel. For each sub-grid column, the IR radiance at the TOA is calculated from a satellite's field of view, including emission/absorption of surface, water vapor and clouds at all levels, while cloud optical properties (visible optical depth and IR emissivity) are determined from the model's cloud water/ice content and droplet/crystal size distribution. The IR radiance from cloud is then determined. The cloud-top temperature is computed using inverse Planck function and cloud-top pressure is determined as the model level with the same temperature. The occurrence frequencies of a variety of cloud types defined by cloud visible optical depth and cloud-top pressure, following the definitions of ISCCP, are then calculated by the ISCCP simulator.

Unlike a general circulation model/SCM, a CRM explicitly simulates two-dimensional (2D) or three-dimensional (3D) cloud fields, so no overlap assumption is needed to get a cloud distribution. We modified the original ISCCP simulator for use in our CRM analysis. Each CRM grid column is considered as a satellite pixel and has a single cloud type.

To calculate the visible (0.65 μm) cloud optical depth and cloud IR (10.5 μm) emissivity due to the CRM simulated liquid water clouds, we used the parameterization of Hu and Stamnes with the cloud droplet effective radius specified as 10 μm. For ice clouds, we used the parameterization of Fu and Liou (1993). The CRM included two different sizes of ice crystals: $r_e = 25$ μm and 75 μm, which represent small ice crystals and "snow" (large ice crystals) respectively. For mixed phase clouds, the visible optical depths of liquid water droplets and ice crystals are added to obtain the total visible optical depth, while the absorption coefficients of cloud droplets and ice crystals are added to obtain the total cloud absorption coefficient used for calculating the LW emissivity. We determined the corresponding cloud type frequencies in the CRM simulation using the modified ISCCP cloud type simulator program every 5 min. Cloud type occurrence frequency is defined as the fraction of model columns that contain each cloud type.

We focus our analysis on the ABC subperiods (14 days) during which cloud formed/decayed mainly within the ARM CART site. Since the satellite cloud-detection and cloud-property retrieval used by Minnis' group are different in night and day, we examine the time-averaged cloud type frequencies during the daytime and nighttime, separately. Due to larger uncertainties in the satellite retrievals around sunrise and sunset, we exclude these times and define daytime as from 0800 to 1700 local time and nighttime as 2000 to 0040. Because the satellite cloud-property retrieval method used for nighttime can not accurately derive the values of τ greater than 10 and most very thin clouds with optical depth (τ) less than 0.1 are not detected at any time, and that most clouds during the IOP are high clouds, we grouped the clouds into eight types (Figure 1): four high-level types: very thin (τ: 0.1 - 1.3), thin (τ: 1.3 - 3.6), moderate (τ: 3.6 - 9.4), and thick (τ >9.4), 2 mid-level and low-level types: thin (τ: 0.1 - 9.4) and thick (τ >9.4). Note that the cloud names used in Figure 1 and hereafter are for convenience; they are different from conventional definitions of optically "thin," "moderate," and "thick" clouds.

The MMCR observed cloud amount is the cloud occurrence frequency (COF) averaged. The COF is computed using the MMCR merged moments and MPL data at about 39 sec intervals. Based on the mean profile of pressure during the entire IOP, the height of 680 mb level is about 3.0 km and that of the
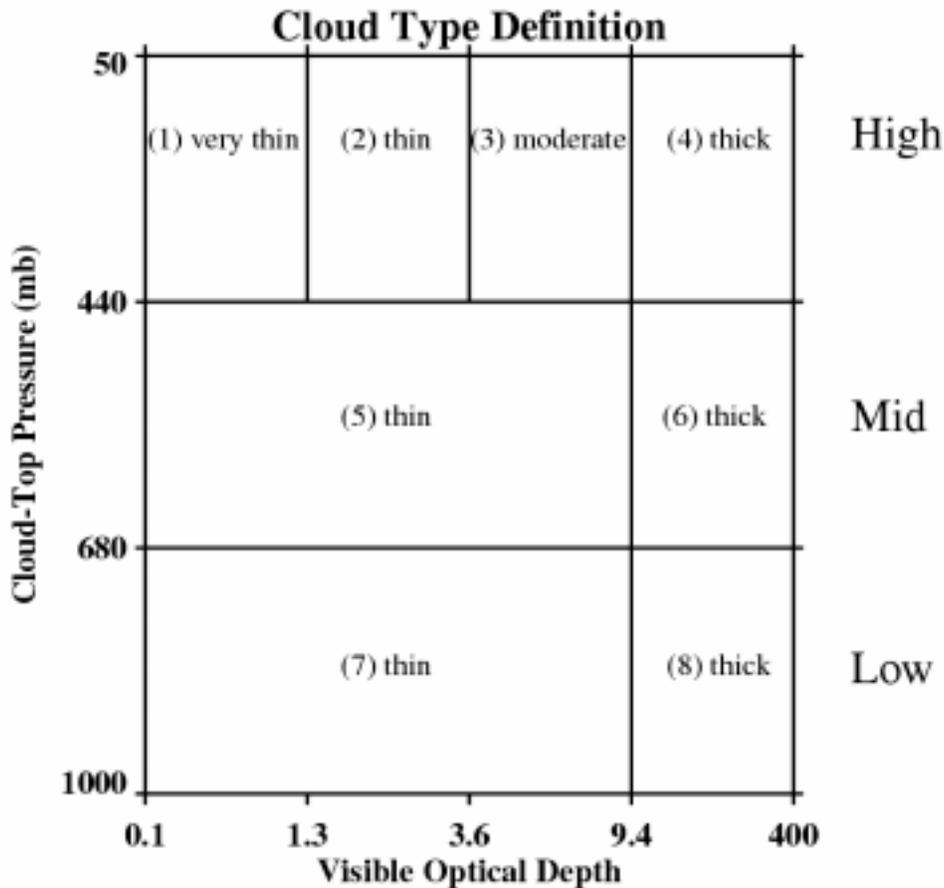

Figure 1. The cloud types defined by cloud visible optical depth and cloud-top pressure used in this study.

440 mb level is about 6.5 km above the ground. We then define the MMCR observed clouds with highest-tops above 6.5 km above the ground as high clouds, between 3.0 and 6.5 km as mid-level clouds, and below 3.0 km as low-level clouds and compute their frequencies respectively.

Cloud Occurrence Frequency: Comparison Among Observations and CRM Simulation

Total Cloud Amount

Table 1 provides a comparison of the total cloud amounts averaged during daytime and nighttime of the ABC subperiods from the MMCR, Minnis, and the CRM simulation. The two CRM cloud amounts: one including clouds with visible optical depth less than 0.1 and the other not, are computed. The former (CRM1) should be compared to the MMCR results, while the latter (CRM2) to Minnis. The total nighttime cloud amount from Minnis data (.52) is close to the MMCR observations (.55), but .12 lower than the MMCR observations in daytime (.42 vs. .54). The CRM total cloud amounts are .42 during day and .40 during night, lower than the MMCR with nearly equal amounts in nighttime and daytime. Compared to Minnis, the CRM cloud amounts for τ_{vis} greater than 0.1 are lower too. The ratio of cloud amounts in daytime and nighttime (Table 2) from the MMCR observations is 1.0, while that from the CRM simulation is 1.0 and Minnis is 0.8. This suggests that Minnis missed some cloud occurrence during daytime and the CRM simulated correct diurnal cycle of total cloud amount though underestimated total cloud amount.

Table 1. The total cloud amount during daytime and nighttime of ABC subperiods from MMCR, Minnis, and the CRM simulation.				
	MMCR	**Minnis**	**CRM1**	**CRM2**
DAY	.54	.42	.42	.36
NIGHT	.55	.52	.40	.35

Table 2. The day/night ratios of total cloud amounts and high cloud amounts during the ABC subperiods from MMCR, Minnis, and the CRM simulation.			
	MMCR	**Minnis**	**CRM**
All Clouds	1.0	0.8	1.0
High Clouds	0.9	0.5	1.0

High-, Mid-, and Low-Level Cloud Amounts

The cloud amounts at high-, mid- and low-levels averaged over the ABC subperiods from the MMCR, Minnis, and the CRM (including/excluding clouds with $\tau < 0.1$) are shown in Table 3. We computed two versions of the CRM high-, mid-, and low-level cloud amounts. In one version, the CRM high-, mid-, and low-level clouds are defined as the highest level with reflectivity greater than -40 dBz_e above 6.5 km, between 3.0 and 6.5 km, and below 3.0 km, respectively. This version (CRM1) is comparable to the MMCR observations. Results from the other version (CRM2) were calculated using ISCCP simulator for clouds with optical depth greater than 0.1 and are comparable to Minnis data.

Table 3. The time-averaged cloud amounts (%) at high-, mid-, and low-levels from the MMCR (MR), Minnis (MS), and the CRM simulation (C1 and C2) during daytime and nighttime of ABC subperiods.											
	High				**Middle**				**Low**			
	MR	**MS**	**C1**	**C2**	**MR**	**MS**	**C1**	**C2**	**MR**	**MS**	**C1**	**C2**
DAY	48	26	37	30	4	8	3	4	2	8	2	2
NIGHT	53	48	37	30	1	3	3	4	1	1	0	1

The 10% difference of daytime Minnis total cloud amount from MMCR results from its 22% difference in the daytime high cloud amount. The ratio of Minnis day/night high cloud amounts (Table 2) is 0.5, lower than the MMCR (0.9) and the CRM (1.0). The Minnis mid- and low-level cloud amounts are larger than MMCR observations, particularly in daytime (16% vs. 6%). We conclude that about half daytime high clouds were missed and/or misclassified as mid- and low-level clouds by the satellite retrieval, and that Minnis cloud amounts are more reliable at night than in the day.

The CRM reproduced the predominance of high clouds: high clouds are 88% of the total cloud amount in daytime and 93% in nighttime while the fractions from the MMCR are 89% and 96%. The CRM also reproduced the same diurnal cycle of high cloud occurrence as the MMCR observations: day/night high cloud amounts ratio is 1.0, almost the same as the MMCR (0.9). However, the CRM simulation underestimated the high cloud amount by 0.11 in daytime and 0.16 in nighttime. One possible reason for the underestimation of CRM's high cloud amount is the lack of large-scale advection of clouds. Too large a fall-speed of large ice crystals could contribute to lower cirrus cloud amount in the CRM. Too low vertical resolution at mid- and upper-troposphere of the simulation (600 to 800 m) and large-scale forcing data (50 mb) could miss some shallow clouds. Other deficiencies of the model and errors in the large-scale forcing data used to drive the model are also possible reasons

Amounts of Cloud Types

We can compare the CRM frequencies of cloud types defined by optical depth with Minnis data only because cloud visible optical depth retrieved from cloud radar combined with other information is available only for very thin and thin cirrus. Figure 2 provides the daytime and nighttime amounts of the eight cloud types shown in Figure 1 for Minnis and the CRM. It shows that the large decrease (0.22) of Minnis high cloud amount from nighttime to daytime occurs for the optically thin high clouds (types 1, 2, and 3), particularly those with between 0.1 and 1.3 (which decreases by 0.14), while the thick high cloud amount remains the same. These indicate that the satellite retrieval used for daytime missed some optically thin high clouds and misclassified some as mid-level and low-level clouds, so that the Minnis thin cloud amounts are more reliable during night than in daytime, and Minnis daytime cloud amount is more reliable for optically thick clouds than for optically thin clouds.

Compared to Minnis data at night and thick cloud amounts in daytime, the CRM (a) thick high cloud amount during daytime is lower by 0.03; (b) optically very thin to moderate high cloud amounts at night is lower by 0.12. In addition to previously discussed reasons, the specified r_e has possible impact on the CRM cloud amounts. The MCA's values, which are similar to the CRM's (Luo et al. 2003), may be too large. The CRM simulation had an amount of 0.06 (daytime) and 0.05 (nighttime) for cloud with τ_{vis} less than 0.1. Using a smaller value of r_e for thin clouds would increase τ and hence change the amounts of cloud types. Particularly high thick cloud amount would increase.
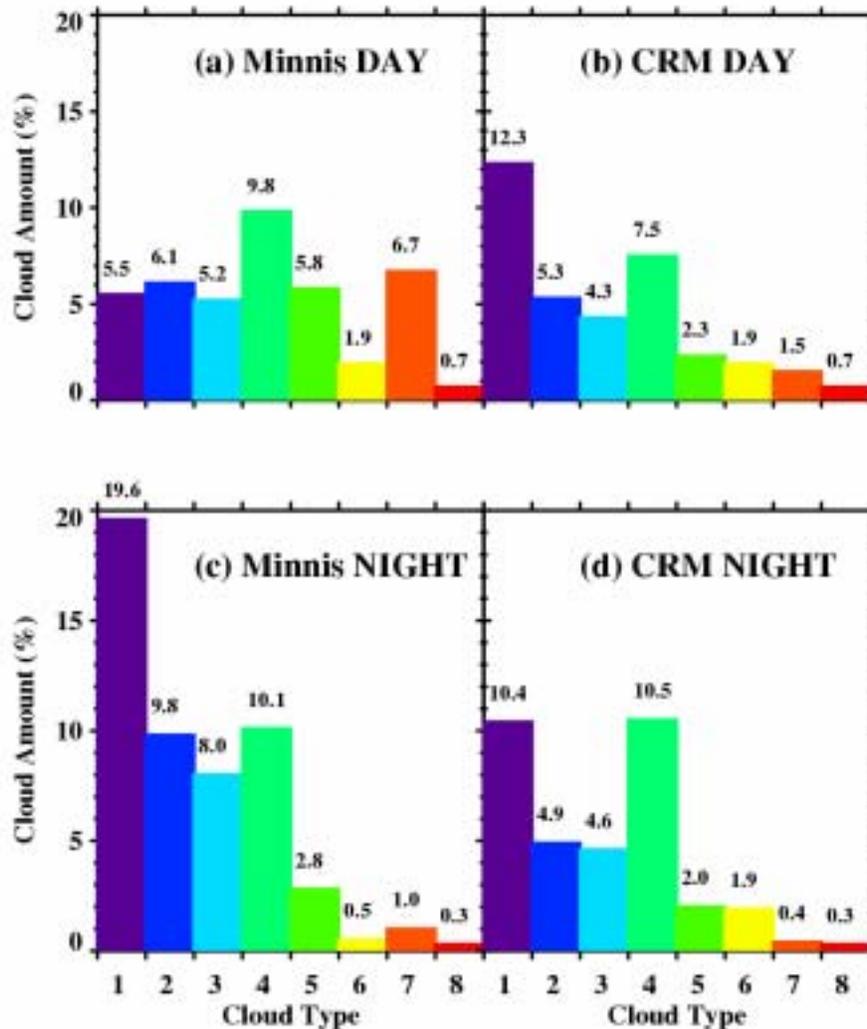
Figure 2. The time-averaged cloud amounts (%) for the eight cloud types from Minnis and the CRM simulation during the selected subperiods A, B, and C. The value above each bar is the corresponding cloud amount. (a) Minnis daytime. (b) CRM daytime. (c) Minnis nighttime. (d) CRM nighttime.

The diurnal cycles of the eight cloud type amounts (Figure 3) show a dramatic change in Minnis data around sunrise and sunset for very thin high clouds and a lesser change for thin high clouds. This, in conjunction with the comparison to MMCR observations, indicates again that there is a systematic bias in the daytime detection by satellite retrieval of very thin and thin high clouds. The CRM nighttime very thin to moderate high cloud amounts are lower than Minnis data. Possible reasons, as discussed previously, include a single 2D simulation, large ice crystals falling too fast, too low vertical resolution at high-level, and lack of large-scale hydrometers advection. Compared to Minnis data, the CRM simulated too low amounts of mid- and low-level thin clouds. This is partly due to Minnis' overestimation in daytime. The CRM turbulence condensation scheme was not used in the simulation, so that small cumulus could not be simulated. This could result in less thin clouds at low- and mid-levels. The CRM seems to underestimate thick high cloud amount in the morning (06 to 12 hr local
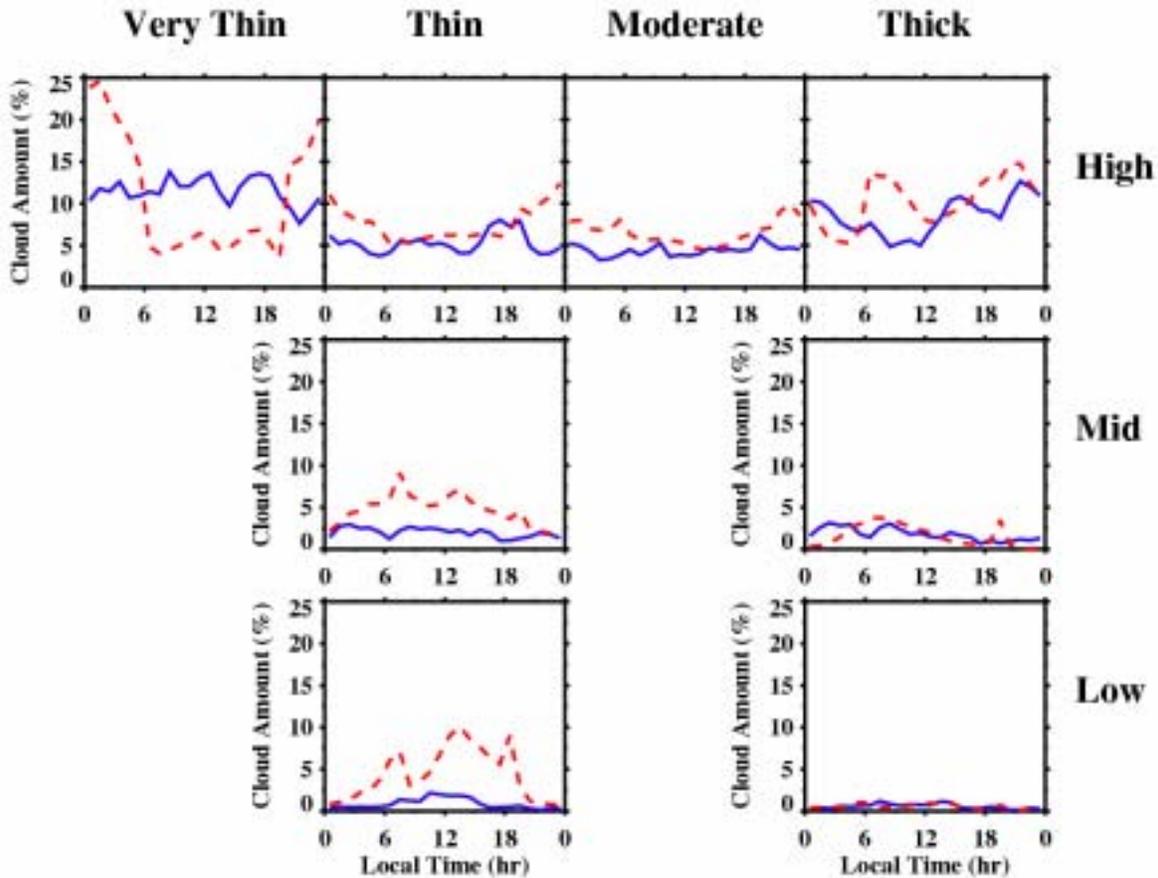
Figure 3. The amounts of various cloud types from Minnis (red lines) and the CRM simulation (blue lines) composited at each hour of day during the selected subperiods A, B, and C.

time) and in early night (18 to 21 hr), and slightly overestimate it late night (01 to 05 hr). Both Minnis and the CRM show very few amounts of thick mid- and low-level clouds.

Using Minnis and the CRM 3 hr time-series of each of the eight cloud type amounts for the entire IOP and the subperiods A, B, and C, we computed the temporal correlations between the CRM and Minnis, as well as the CRM normalized standard deviations. These results are illustrated using Taylor diagrams (Figure 4). Except for thin clouds at mid-level (green symbol '5' in Figure 3) and thick clouds at low-level (red symbol '8'), the correlations of the CRM cloud type amounts with Minnis data are better during the ABC subperiods than the entire IOP. The improvement is significant for high clouds (blue symbol 'H', 0.36 to 0.67) while correlations remain almost the same for mid- and low-level clouds (green symbol 'M' and red symbol 'L', 0.58 to 0.53 and 0.42 to 0.47, respectively), and the improvement is more obvious for thin clouds (black symbol 't', 0.16 to 0.47) than thick clouds (black symbol 'T', 0.62 to 0.66). During the entire IOP and the ABC subperiods, thick high clouds have the best correlation with Minnis (0.59 and 0.64), and thick mid-level clouds have the second best correlation (0.59 and 0.62), while very thin high clouds have the worst correlation (-0.02 and 0.18). These results are expected considering that thick clouds generated by local convection are mostly formed and dissipated locally while very thin cirrus with longer life time usually have larger large-scale advection,
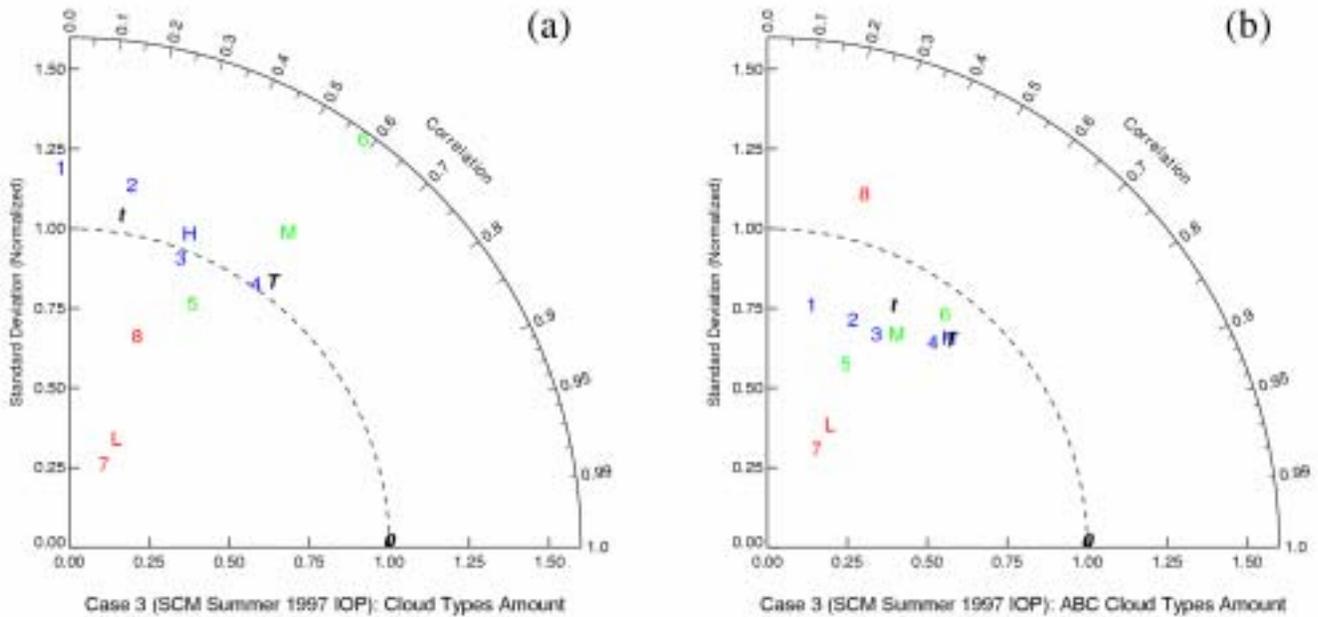
Figure 4. Taylor diagrams for the CRM 3-hourly occurrence frequencies of various cloud types. (a) The entire IOP. (b) The subperiods A, B, and C. Blue symbols are high cloud types: 1 is very thin, 2 is thin, 3 is moderately thick, 4 is thick, and H is all high clouds. Green symbols are mid-level cloud types: 5 is thin, 6 is thick, and M is all mid-level clouds. Red symbols are low-level cloud types: 7 is thin, 8 is thick, and L is all low-level clouds. Black **T** is thick clouds, and **t** is thin clouds. The reference fields are the corresponding cloud type frequencies from Minnis data.

which is not included in the simulation, and also Minnis very thin and thin cirrus amounts are unreliable in daytime. During ABC subperiods, the CRM cloud type amounts have too small normalized standard deviation particularly the thin clouds at mid- and low-levels, except for the thick low-level clouds.

Cloud Radiative Forcing

Definition of Cloud Radiative Forcing

We are aware that cloud processes are internal to the climate system and interact strongly with other climate processes while the term "forcing" usually refers to an external process. However, the term "cloud radiative forcing" (CRF) is defined here as the difference between the absorbed radiative flux under all-sky and clear-sky conditions:

$$CRF = H - H_{clr} \qquad (1)$$

Where H is the radiation absorbed by the earth-atmosphere system in a region and H_{clr} is the corresponding clear-sky absorbed radiation. By definition, the CRF is a measure of the impact of clouds on the energy balance of the earth. The absorbed radiation is

$$H = s(1 - \alpha) - OLR = s - OSR - OLR \qquad (2)$$

where s is incident solar radiation, α is albedo, OSR is reflected solar radiation, and OLR is outgoing LW radiation. The CRF is then

$$CRF = (s - OSR - OLR) - (s_{clr} - OSR_{clr} - OLR_{clr}) \qquad (3)$$

where the suffix "clr" indicates the clear-sky fluxes and no suffix refers to all sky fluxes. At the TOA, since, $s_{clr} = s$. we get

$$CRF = (OSR_{clr} - OSR) + (OLR_{clr} - OLR) \qquad (4)$$

The first and second parts of the right-hand-side (r.h.s.) of Eq. (4) are, respectively, the SW CRF and LW CRF. The solar and IR effects of clouds have offsetting effects in terms of the energy balance of our planet. In the LW, clouds generally reduce the radiation emitted to space and tend to heat the planet. In the solar (or SW) clouds reflect more solar radiation, due to generally higher albedo of clouds than the underlying surface, and tend to cool the planet. The net radiative effect of clouds depends on their macrophysical properties (amount, temperature, and vertical distribution) and radiative properties (emissivity and reflectivity), as well as the characteristics of the surface and the atmosphere.

Methods for Analyzing Cloud Radiative Forcing

Method for Analyzing Minnis Data

Using half-hourly Minnis pixel-level data, we averaged the TOA LW flux and SW albedo over the pixels which are within SGP SCM analysis domain and either detected as clear or with reliable retrieval, to get area averaged LWflux and albedo for all-sky, clear-sky, and each of the 8 cloud types shown in Figure 1, respectively. During twilight, the SGP SCM analysis domain is partly daytime and SW albedo is averaged over daytime pixels only. The fractional areas for clear-sky and for each of the 8 cloud types are also computed.

We then linearly interpolated to get TOA LW fluxes, area-averaged SW albedos, and the fractional areas for all-sky, clear-sky, and cloudy-sky at one hour intervals. Since clear-sky LW flux and area-averaged SW albedo are needed for CRF calculations at each hour, values at two available times closest to the interpolated time are used for interpolation. The hourly averaged SW upward flux is calculated from the SW albedo (α), using

$$OSR = \alpha s = \alpha \times S \times \left(\frac{d_m}{d} \right)^2 \times \cos(\theta) \qquad (5)$$

where S (1366 W/m^2) is the solar constant at the mean sun-earth distance (d_m), d is the instantaneous sun-earth distance, θ is the hourly averaged solar zenith angle. For each hour of the IOP, the values of

$\cos(\theta)$ and $\dfrac{d_m}{d}$ and at the SGP CF are computed by integrating over 6 even time windows, i.e., each window is 10 min.

The hourly overcast CRF is the difference in radiative fluxes between overcast and clear conditions, while CRF is obtained by weighting the overcast CRF by the cloud amount. We calculated the hourly LW and SW overcast CRFs and CRFs for each cloud type at each hour.

CRM Radiation Calculation

We calculated the LW and SW fluxes at TOA from the cloud and atmospheric fields simulated by the CRM using the radiative transfer (RT) model developed by Fu and Liou (1992, 1993). In this radiation code, 6 and 12 bands are used for solar and thermal IR regions, respectively.

The required inputs to the RT model at the surface include SW spectral albedo, IR spectral emissivity, and skin temperature. The 3-hourly broadband surface albedo was computed using the broadband downward and upward surface fluxes from Solar and Infrared Observation Station (SIROS) measure–ments at the SGP CART site. These were averaged for each 3 hr of daytime over the whole IOP to get the mean values. We linearly fitted the broadband albedo (α) as a function of $\cos(\theta)$ and used the fit to obtain the spectral albedo: $c\alpha$, while c is 0.428, 1.507, and 1.542 for wavelength of 0.2 - 0.7, 0.7 - 1.3, and 1.3 - 4.0 µm, respectively. The surface is considered in 80% grass and 20% shrub.

We calculated the surface skin temperature (T_s) from the downward (F_{dn}) and upward (F_{up}) LW flux measurements by SIROS using the following formula, assuming that the surface emissivity (ε) is 0.98,

$$T_s = \left(\frac{F_{up} - (1-\varepsilon)F_{dn}}{\varepsilon\sigma} \right)^{0.25} \tag{6}$$

where σ is the Stefan-Boltzmann constant. The domain averaged 3 hr T_s is interpolated to get the values at 5 min intervals. At each 5 min, the domain averaged T_s is used for all grid columns.

The r_e used is 10 µm for liquid water droplets, 25 µm for small ice crystals, and 75 µm for large ice crystals ("snow"). The surface water vapor mixing ratio is obtained from the observed time-varying temperature and relative humidity at 2 m above the ground. The solar insolation (s) as another required input is computed every 5 min including the variation of earth-sun distance (d) and solar zenith angle (θ).

The TOA LW and SW fluxes for all-sky are simply the averages over the entire CRM domain. To get the TOA clear-sky fluxes, we selected fluxes at columns without cloud or containing cloud with τ less than 0.1. This is reasonable since such optically thin clouds were mostly missed by the satellite retrieval and their radiative effects are negligible. The amount and TOA fluxes from each of the eight cloud types were also determined. We computed the LW and SW overcast CRFs and CRFs, and the net CRF the same as for the Minnis data. Again, we focus our analysis for the selected subperiods A, B, and C.

Cloud Radiative Forcing: Comparison between Minnis and CRM

Clear-Sky Fluxes

We compared the CRM and Minnis clear-sky fluxes during the ABC subperiods by compositing them at each hour of the day. The TOA CRM reflected SW flux is larger than Minnis flux. When averaged over daytime (0800 to 1700 local time), Minnis reflected SW flux at TOA is 169.7 W/m^2, while the CRM's is 188.3 W/m^2. This indicates about 0.02 difference in albedo (11% of Minnis clear-sky albedo). We suspect that the surface albedo used in our CRM radiative transfer calculation is too large. The SIROS measured the surface fluxes at 6 locations within the SGP CART site. The albedo at those locations may be larger than the average over the whole SGP CART site. The clear-sky OLR in the CRM appears to have a weaker diurnal signal than observed. Minnis clear-sky OLR is 302.7 W/m^2 in daytime and 284.2 W/m^2 in nighttime, compared to the CRM's 295.6 W/m^2 and 287.9 W/m^2. The amplitudes are 18.5 W/m^2 (Minnis) and 7.7 W/m^2 (CRM). The 7 W/m^2 difference in daytime OLRs from Minnis and the CRM corresponds to about 1oK difference in effective radiating temperatures. Possible reasons for differences in diurnal amplitude of clear-sky OLRs include (a) the skin temperature derived from the SIROS measurements may be not representative of the entire SGP CART site; (b) clear- and cloudy-sky OLRs differ in nature: clear-sky OLR is larger/smaller than cloud-sky OLR in daytime/nighttime. However, the CRM used the same area-averaged skin temperature for each grid column. This could decrease/increase estimated daytime/nighttime clear-sky OLR and hence reduce the amplitude of diurnal cycle.

Overcast CRFs of Various Cloud Types

Minnis data show that high and/or thick clouds have larger LW overcast CRFs than lower and/or thinner clouds. The cloud types in descending order of LW CRF are thick high, moderate high, thin high, thick mid-level, very thin high, thin mid-level, thick low-level, and thin low-level. The CRM reproduced these results.

For both Minnis and the CRM, optically thicker clouds reflect more SW flux than thinner clouds for the same cloud amount. The cloud types in descending order of SW overcast CRF are thick high, thick mid-level, thick low-level, moderate high, thin high, thin mid-level, thin low-level, and very thin high. The CRM cloud types have smaller SW overcast CRFs than do their counterparts measured by Minnis. The differences are within 25 W/m2 and mainly because of 18 W/m^2 larger CRM clear-sky SW reflected flux, except for thick low-level cloud whose CRF is - 73 W/m^2 smaller than Minnis. However, there may be large uncertainty in SW flux from this cloud type in Minnis data since the occurrence of such clouds is only 0.01 during daytime of ABC subperiods.

CRFs Under Observed/Simulated Cloud Amounts

Figures 5 to 7 provide the LW, SW, and net CRFs of each cloud type averaged over the ABC subperiods including twilights from Minnis and the CRM. Basically, the CRM simulation reproduced the major features of LW, SW, and net CRFs as estimated from the satellite data, though noticeable differences exist. The CRM LW CRFs of optically thin to thick high clouds and mid- and low-levels thin clouds (types 2, 3, 4, 5, and 7) are smaller than Minnis due to lower amounts simulated, while the CRM LW
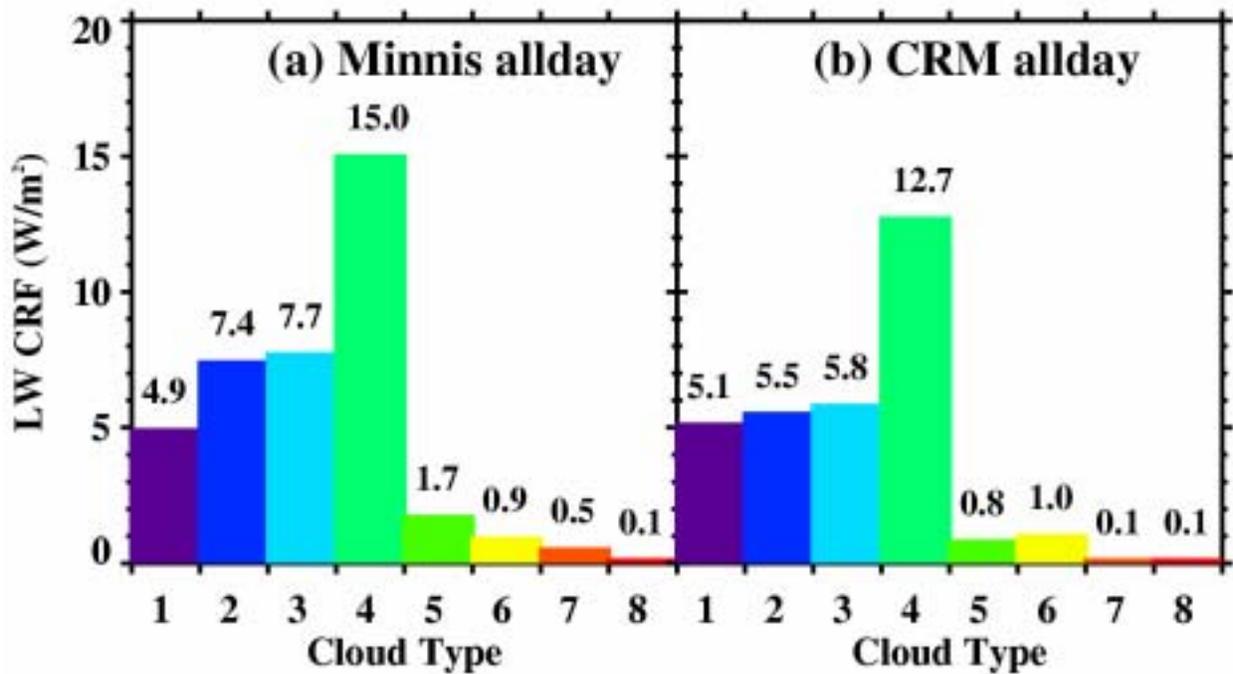
Figure 5. The longwave cloud radiative forcings (CRFs) of the eight cloud types during the subperiods A, B, and C from (a) Minnis data and (b) CRM results. The value above each bar is the LW CRF for that cloud type.
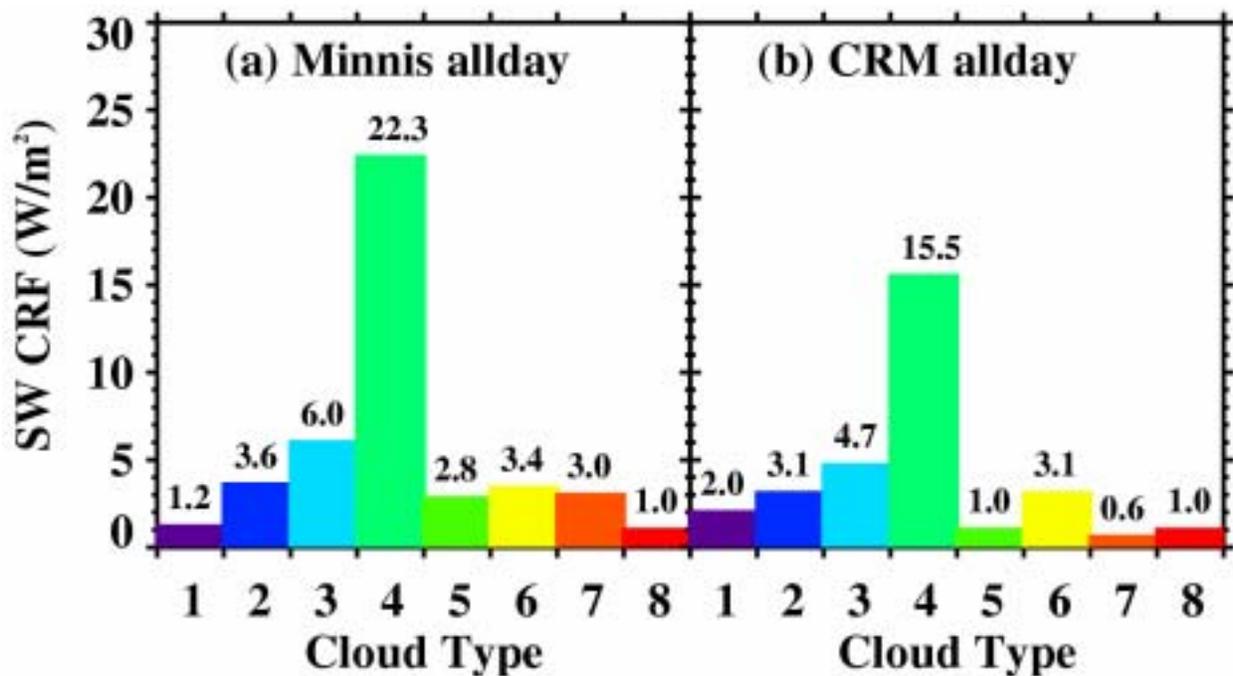

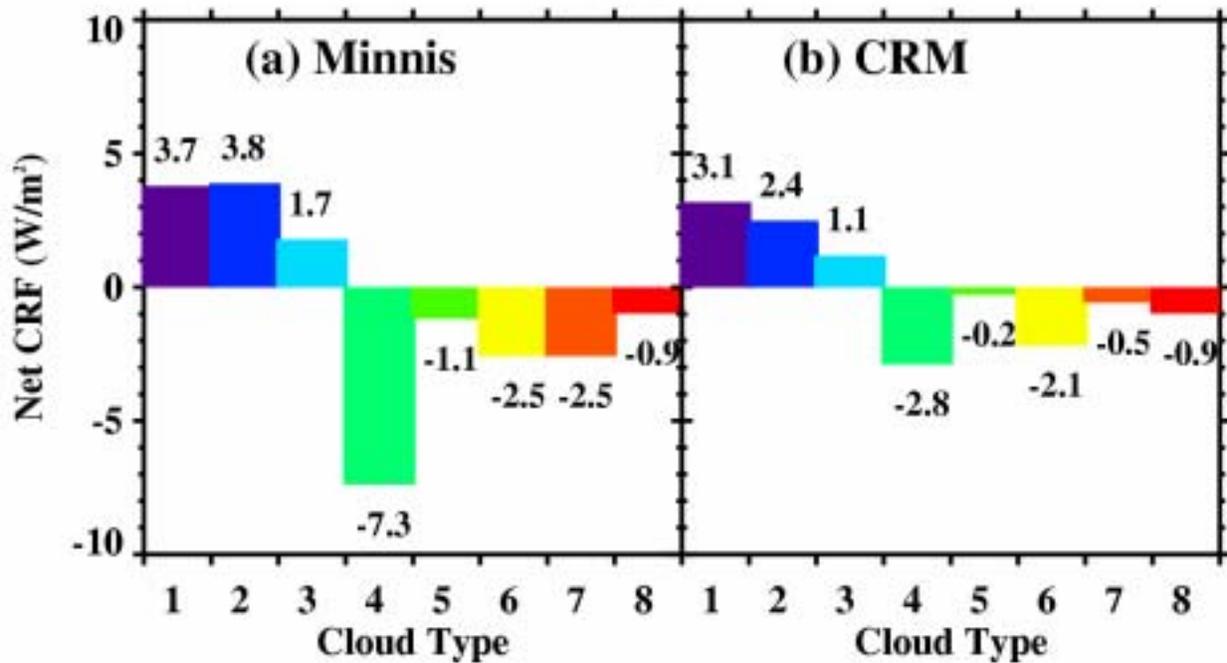**Figure 6**. Similar to Figure 5 but for shortwave CRF.

Figure 7. Similar to Figure 5 but for the net cloud radiative forcing: LW CRF – SW CRF.

CRFs of other cloud types are almost the same as Minnis. It is interesting that the CRM SW CRFs of cloud types 2, 3, 4, 5, and 7 are smaller than Minnis, as found for their LW CRFs. The differences between the CRM and Minnis SW CRFs of cloud types 4, 5, and 7 (-6.8, -1.8, and -2.4 W/m^2) are more significant than the corresponding differences in LW CRFs (-2.3, -0.9, and -0.4 W/m^2), due to larger overcast SW CRFs than overcast LW CRFs of these cloud types. Similarly, the differences between the CRM and Minnis SW CRFs of cloud types 2 and 3 (-0.5, -1.3 W/m^2) are less significant than the corresponding differences in LW CRFs (-1.9 and -1.9 W/m^2), due to smaller overcast SW CRFs than overcast LW CRFs of these cloud types.

The net CRFs (Figure 7) of optically very thin to moderate high clouds (types 1, 2, and 3) are warming, while other cloud types are cooling and thick high clouds had the largest cooling effect, as revealed by both Minnis and the CRM. However, the CRM cloud types 4, 5, and 7 have less significant cooling effect (-2.8, -0.2, and -0.5 W/m^2) than Minnis (-7.3, -1.1, and -2.5 W/m^2), while the CRM cloud types 2 and 3 have less significant warming effect (2.4 and 1.1 W/m^2) than Minnis (3.8 and 1.7 W/m^2). Table 4 provides the CRFs by all cloud types as a whole from Minnis and the CRM. The LW and SW CRFs estimated from Minnis data are 38 and -43 W/m^2, respectively, while the CRM simulation had smaller absolute values (31 and -31 W/m^2). As a result, the net CRF is -5 W/m^2 from Minnis and 0W/m^2 from the CRM simulation.

Summary and Discussion

Comparing the CRF and cloud amount from a model simulation with observations is a traditional way in model evaluation. However, CRF and cloud amount alone do not give many clues about the causes of

difference/similarity between models and observations. We have evaluated clouds in a CRM in a way that dissects TOA CRF and cloud amount into cloud type distributions, which reveals much more cloud information than the traditional method does. We used data from cloud radar observations and geostationary satellite pixel-level cloud products from Minnis' group at NASA Langley Research Center at the ARM SGP CART site to evaluate the occurrence frequencies and radiative effects of various cloud types in a CRM simulation for the summer 1997 IOP. Such a study has not been done before mainly because of lack of observations at resolution comparable to a CRM's grid.

To compare with MMCR observations of cloud occurrence, we defined cloud boundaries by reflectivity of hydrometers. The CRM reproduced the dominance of high cloud, but underestimated high cloud occurrence by 0.13 compared to the MMCR observations. The lack of large-scale advection of cloud condensation, errors in the large-scale forcing data, limitation of one single 2D simulation, too low vertical resolution at mid- and high-troposphere of both the CRM simulation and the large-scale forcing data, large ice crystals falling too fast, and other defects in model's formulations are all possible reasons.

To compare with satellite data, the ISCCP simulator was used to analyze the CRM results. The CRM simulation reproduced the cloud type distribution estimated from satellite data. The simulated thick cloud temporally correlated better with the satellite observations (0.67 and 0.62 during ABC subperiods and entire IOP) than thin cloud (0.47 and 0.16 during ABC subperiods and entire IOP), partly due to less large-scale advection of thick clouds and partly because daytime satellite thin cloud amount is unreliable. The improvements in ABC subperiods compared to entire IOP result from less large-scale cloud advection, also.

The CRM reproduced the overcast LW and SW CRFs of various cloud types obtained from the satellite observations. Both Minnis data and the CRM suggest that the net CRF of the optically thin high clouds had a warming effect at the TOA, while the other cloud types had a cooling effect. The thick high cloud had the most significant cooling effect.

The net CRF averaged over ABC subperiods by all cloud types from Minnis data and the CRM is -5 and 0 W/m^2, respectively. How significant is the difference? To answer this question, uncertainties of both the satellite CRF and the CRM CRF are needed. For the former, we can compare the Minnis CRF with CRF from other data sources, such as ISCCP. However, the ISCCP pixel-level cloud products contain only about 70 pixels within the SGP SCM analysis domain and at 3 hr intervals. Therefore, there maybe large sampling errors in the derived CRFs. The sampling errors of the ISCCP values could be determined by sub-sampling Minnis in the same way many times to get an ensemble of measurements. This could be done for a single time to determine spatial sampling errors, or for time averages to determine temporal and spatial sampling uncertainties. For the latter, one of the methods is making an ensemble of the CRM simulations using different random seeds and then analyzing the uncertainties of the ensemble mean values. Another method is sub-sampling the CRM simulation results to get multiple datasets and then examine the uncertainties of the mean values. Quantifying these uncertainties is a meaningful future work.

The specified r_e/D_e in the CRM radiation calculation could produce uncertainty. The values used maybe too large. Using smaller values could change cloud type amounts, e.g., increase thick high cloud

amount. More accurate values from observations are desired. It would also be interesting to quantify the CRM uncertainty caused by the specified droplet/crystal size.

It is demonstrated that data from satellite retrieval and radar observations complement each other. The pixel level satellite data can be used to evaluate the occurrence frequencies and radiative effects of various cloud types in a CRM, while radar observations can help determine the uncertainties in satellite retrieval. For example, we found that about half daytime thin high clouds were missed and/or misclassified as lower-level clouds by the satellite retrieval. For a CRM embedded in a general circulation model, i.e., a CRM is used as a super-parameterization in a general circulation model; we can apply this method—combining radar and satellite observations—to the sites/general circulation model grid columns where a MMCR is located. It is obvious that this method can be applied to a SCM, too.

References

Barkstrom, B. R., 1984: The Earth Radiation Budget Experiment (ERBE). *Bull. Am. Meteorol. Soc.*, **65**, 1170-1185.

Cess, R. D., et al., 1996: Cloud feedback in atmospheric general circulation models: An Update. *J.* Geophys. Res., **101**,12,791-12,794.

Chaboureau, J., and P. Bechtold, 2002: A simple cloud parameterization derived from cloud resolving model data: Diagnostic and Prognostic Applications. *J. Atmos. Sci.*, **59**, 2362-2372.

Chen C.-T., and R. Erich, 1995: Validation of the Earth radiation budget as simulated by the Max-Planck-Institute for Meteorology general circulation model ECHAM4 using satellite observations of the Earth Radiation Budget Experiment (ERBE). Hamburg, Germany, Max-Planck-Institut fuer Meteorologie, p. 56.

Chen, T., W. B. Rossow, and Y.-C. Zhang, 2000: Radiative effects of cloud-type variations. *J. Climate.*, **13**, 264-286.

Dong, X., and G. G. Mace, 2003: Profiles of low-level stratus cloud microphysics deduced from ground-based measurements. *J. of Atmospheric and Oceanic Technology*, **20**, 42-53.

Fu, Q., and K. N. Liou, 1992: On the correlated k-distribution method for radiative transfer in nonhomogeneous atmospheres. *J. Atmos. Sci.*, **49**, 2139-2156.

Fu, Q., K. N. Liou, 1993: Parameterization of the radiative properties of cirrus clouds. *J. Atmos. Sci.*, **50**, 2008–2025.

Han, W., K. Stamnes, and D. Lubin, 1999: Retrieval of surface and cloud properties in the Arctic from NOAA AVHRR measurements. *J. Appl. Meteor.*, **38**, 989-1012.

Harrison, E. F., P. Minnis, B. R. Barkstrom, V. Ramanathan, R. Cess, and G. G. Gibson, 1990: Seasonal variation of cloud radiative forcing derived from the Earth Radiation Budget Experiment. *J. Geophys. Res*., **95**, 18,687-18,703.

Hartmann, D. L, L. A. Moy, and Q. Fu, 2001: Tropical convection and the energy balance at the top of the atmosphere. *J. Climate*, **14**, 4495-4511.

Hartmann, D. L., M. E. Ockert-Bell, and M. L. Michelsen, 1992: The Effect of Cloud Type on Earth's Energy Balance: Global Analysis. *J. Climate*, **5**, 1281–1304.

Khairoutdinov, M. F., and D. A. Randall, 2001: A cloud resolving model as a cloud parameterization in the NCAR community climate system model: Preliminary Results. *Geophys. Res. Lett*., **28**, 3617-3620.

Luo, Yi, et al., 2003: Surface bi-directional reflectance properties over the ARM SGP area from satellite multi-platform observations. This Proceedings.

Khaiyer, M. M., et al., 2002: Evaluation of a 5-year cloud and radiation property dataset derived from GOES-8 data over the Southern Great Plains. In *Proceedings of the Twelfth Atmospheric Radiation Measurement (ARM) Science Team Meeting*, ARM-CONF-2002. U.S. Department of Energy, Washington, D.C. Available URL: http://www.arm.gov/docs/documents/technical/conf_0204/khaiyer-mm.pdf

Kiehl, J. T., J. J. Hack, and B. P. Briegleb, 1994: The simulated earth radiation budget of the National Center for Atmospheric Research community climate model CCM2 and comparisons with the Earth Radiation Budget Experiment (ERBE). *J. of Geophy. Res*., **99**, 20,815-20,827.

Kohler, M., 1999: Explicit prediction of ice clouds in general circulation models. Ph.D. dissertation, University of California, Los Angeles, p. 67. Available from Department of Atmospheric Sciences, University of California, 405 Hilgard Avenue, Los Angeles, California 90095.

Krueger, S. K., G. T. McLean, and Q. Fu, 1995: Numerical simulation of the stratus-to-cumulus transition in the subtropical marine boundary layer. Part I: Boundary-Layer Structure. *J. Atmos. Sci*., **52**, 2839-2850.

Luo, Y.-L., S. K. Krueger, G. G. Mace, and K.-M. Xu, 2003: Cirrus cloud statistics from a cloud-resolving model simulation compared to cloud radar observations. *J. Atmos. Sci*., **60**, 510-525.

Mace, G. G., E. E. Clothiaux, and T. P. Ackerman, 2001: The composite characteristics of cirrus clouds; bulk properties revealed by one year of continuous cloud radar data. *J. Climate*, **14**, 2185-2203.

Minnis, P., D. P. Garber, D. F. Young, R. F. Arduini, and Y. Takano, 1998: Parameterizations of reflectance and effective emittance for satellite remote sensing of cloud properties. *J. Atmos. Sci*., **55**, 3313-3339.

Minnis, P., W. L. Smith, D. P. Garber, J. K. Ayers, and D. R. Doelling, 1995a: "Cloud properties derived from GOES-7 for the spring 1994 ARM Intensive Observing Period using Version 1.0.0 of the ARM satellite data analysis program," NASA Tech. Rep. RP 1366, p. 59.

Minnis, P., D. P. Kratz, J. A. Coakley, Jr., M. D. King, D. Garber, P. Heck, S. Mayor, D. F. Young, and R. Arduini, 1995b: Cloud optical property retrieval (Subsystem 4.3). "Clouds and the Earth's Radiant Energy System (CERES) algorithm theoretical basis document, Volumn III: Cloud analyses and radiance inversions (Subsyatem 4)," NASA Tech. Rep. RP 1376, 135-176.

Platnick, S., J. Y. Li, M. D. King, H. Gerber, and P. Hobbs, 2001: A solar reflectance method for retrieving the optical thickness and droplet size and liquid water clouds over snow and ice surfaces. *J. Geophys. Res.*, **106**, 15,185-15,199.

Rossow, W. B., and R. A. Schiffer, 1991: ISCCP cloud data products. *Bull. Amer. Meteor. Soc.*, **72**, 2-20.

Rossow, W.B., and R.A. Schiffer, 1999: Advances in understanding clouds from ISCCP. *Bull. Amer. Meteor. Soc.*, **80**, 2261-2289.

Rossow, W.B., A. W. Walker, D. Beuschel, and M. Roiter, 1996: International Satellite Cloud Climatology Project (ISCCP) description of new cloud datasets. WMO/TD 737,World Climate Research Programme (ICSU and WMO), p. 115.

Senior, C. A., and J. F. B. Mitchell, 1993: Carbon dioxide and climate: the impact of cloud parameterization. *J. of Climate*, **6**, 393-418.

Wang, Z., and K. Sassen, 2002a: Cirrus cloud microphysical property retrieval using lidar and radar measurements. Part I: Algorithm Description and Comparison with In Situ Data. *J. Appl. Meteorol.*, **41**, 218-229.

Wang, Z., and K. Sassen, 2002b: Cirrus cloud microphysical property retrieval using lidar and radar measurements. Part II: Midlatitude Cirrus Microphysical and Radiative Properties. *J. Atmos. Sci.,* **59**, 2291–2302

Webb, M., C. Senior, S. Bony, and J.-J. Morcrette, 2001: Combining ERBE and ISCCP data to assess clouds in the Hadley Center, ECMWF and LMD atmospheric climate models. *Climate Dynamics*, **17**, 905-922.

Young, D. F., P. Minnis, W. L. Smith Jr., and D. P. Garber, 1997: A four-channel method for deriving cloud radiative properties from meteorological satellite data. IRS '96: Current Problems in Atmospheric Radiation, eds., W. L. Smith and K. Stamnes, Deepak, 612-615.

Zhang, Y., R. Burkhardt, S. Rolf, H. Rainer, K. Ute, 2001: REMO Cloud Modeling: Improvements and Validation with ISCCP DX Data. *J. of Applied Meteorology*, **40**, 389-408.